



## OPEN ACCESS

## EDITED BY

Costanza Bonadiman,  
University of Ferrara, Italy

## REVIEWED BY

Stefano Naitza,  
University of Cagliari, Italy  
Sam Uthup,  
National Taiwan Normal University,  
Taiwan

## \*CORRESPONDENCE

Ying-Hui Zhang,  
✉ yhzhang@sina.cn  
Zhuang Li,  
✉ lizhuangcc@pku.edu.cn

RECEIVED 16 January 2023

ACCEPTED 19 June 2023

PUBLISHED 29 June 2023

## CITATION

Zhu W-P, Tian W, Zhang Y-H, Li Z,  
Gong M-Y, Fu B, Wang Z-L and Wei C-J  
(2023), Geological characteristics and  
genesis of the Late Carboniferous  
extremely thick slate in the  
Shuangjianzishan Ag-Pb-Zn district,  
southern Great Xing'an Range, NE China:  
constraints on metallogenesis and  
tectonic setting.  
*Front. Earth Sci.* 11:1145656.  
doi: 10.3389/feart.2023.1145656

## COPYRIGHT

© 2023 Zhu, Tian, Zhang, Li, Gong, Fu,  
Wang and Wei. This is an open-access  
article distributed under the terms of the  
[Creative Commons Attribution License  
\(CC BY\)](https://creativecommons.org/licenses/by/4.0/). The use, distribution or  
reproduction in other forums is  
permitted, provided the original author(s)  
and the copyright owner(s) are credited  
and that the original publication in this  
journal is cited, in accordance with  
accepted academic practice. No use,  
distribution or reproduction is permitted  
which does not comply with these terms.

# Geological characteristics and genesis of the Late Carboniferous extremely thick slate in the Shuangjianzishan Ag-Pb-Zn district, southern Great Xing'an Range, NE China: constraints on metallogenesis and tectonic setting

Wei-Peng Zhu<sup>1,2</sup>, Wei Tian<sup>2</sup>, Ying-Hui Zhang<sup>1\*</sup>, Zhuang Li<sup>3\*</sup>,  
Ming-Yue Gong<sup>4</sup>, Bin Fu<sup>5</sup>, Zi-Long Wang<sup>2</sup> and Chun-Jing Wei<sup>2</sup>

<sup>1</sup>Key Laboratory of Deep-Earth Dynamics of Ministry of Natural Resources, Institute of Geology, Chinese Academy of Geological Sciences, Beijing, China, <sup>2</sup>MOE Key Laboratory of Orogenic Belts and Crustal Evolution, School of Earth and Space Sciences, Peking University, Beijing, China, <sup>3</sup>State Key Laboratory of Petroleum Resources and Prospecting, College of Geosciences, China University of Petroleum (Beijing), Beijing, China, <sup>4</sup>Petroleum Exploration and Production Research Institute, SINOPEC, Beijing, China, <sup>5</sup>Research School of Earth Sciences, The Australian National University, Canberra, ACT, Australia

The Shuangjianzishan super-large Ag-Pb-Zn deposit is situated in the southern Great Xing'an Range (SGXR), which is part of the eastern Central Asian Orogenic Belt (CAOB) and the northeastern Xing'an-Mongolia Orogenic Belt (XMOB). The host rock of this deposit is the Dashizhai Formation, characterized by a widely distributed, extremely thick slate in the Shuangjianzishan basin. Petrographically, the slate contains secondary minerals such as secondary quartz, biotite, sphalerite, pyrite, galena, and chalcopyrite, in addition to primary quartz, feldspar, and rock fragment. The whole-rock geochemical analysis indicates that the slate was deposited in an oxygen-deficient shale basin, influenced by calcium-rich volcanic ash and magmatic-hydrothermal fluids. The mineralogical characteristics of sulfide minerals and the *in-situ* sulfur isotopic composition of pyrites suggest that the sulfide minerals were likely formed before the primary metallogenic epoch, indicating pre-enrichment of metals. The color variation from black to green observed in the drilling core of the slate is attributed to differences in feldspar content, with the denser "black" slate marking the metallogenic horizon. Based on previous research, it is inferred that the slate is a product of the post-orogenic extensional tectonic setting of the XMOB in the Late Carboniferous, and it underwent alteration by epithermal magmatic-hydrothermal fluids during the Mesozoic metallogenic episode.

## KEYWORDS

Central Asian Orogenic Belt, Shuangjianzishan, Late Carboniferous, extremely thick slate, sulfide minerals, magmatic-hydrothermal fluids

## 1 Introduction

The southern Great Xing'an Range (SGXR), located within the eastern Central Asian Orogenic Belt (CAOB), is one of the most significant Cu-Mo-Fe-Sn-Ag-Pb-Zn metallogenic provinces in China (e.g., Zhou et al., 2010; Zeng et al., 2011; Ouyang et al., 2014a; Ouyang et al., 2014b; Zhai et al., 2014a; Zhai et al., 2014b; Zhai et al., 2017; Zhai et al., 2018; Zhai et al., 2020; Mao et al., 2014; Shu et al., 2016; Chen et al., 2017a; Ke et al., 2017; Gao et al., 2018; Wang et al., 2018; Sun et al., 2022). Research conducted over the past decade on ore deposit geochronology, ore body characteristics, and metallogenic mechanisms reveals that Ag-Pb-Zn deposits in this region formed during the Mesozoic metallogenic episode and are hosted in the Late Paleozoic strata (e.g., Zeng et al., 2011; Yang et al., 2014; Ouyang et al., 2015; Ruan et al., 2015; Liu et al., 2016; Zhai et al., 2020). These deposits are generally associated with the epithermal deposition of magmatic-hydrothermal fluids.

The Xing'an-Mongolia Orogenic Belt (XMOB) is the southeastern segment of the CAOB in China and is adjacent to the North China Craton (NCC). The Shuangjiazishan Ag-Pb-Zn deposit, the largest one discovered in China and Asia to date, is located in the SGXR and northeastern XMOB. It contains 145 million metric tons of ore, with grades of 128.5 g/t Ag (locally up to 32,000 g/t) and 2.2 wt.% Pb+Zn (Zhai et al., 2020). Its exploration was recognized as one of the "Top 10 Prospecting Results" in 2018 by the Geological Society of China. Previous studies have primarily focused on the metallogenic epoch, minerogenic stage, metal occurrence, and metallogenic fluid source of the deposit (e.g., Wu et al., 2013; Liu et al., 2016; Wang et al., 2019; Zhang et al., 2019; Zhai et al., 2020), with relatively less attention given to the host rock.

The Dashizhai Formation, widely distributed in the Shuangjiazishan basin, is identified as the host rock of the Shuangjiazishan Ag-Pb-Zn deposit, primarily comprising slate, siltstone, and intermediate volcanic rock. The formation age remains controversial, with the volcanic rock being attributed to the Early Permian (Yu et al., 2017; Zhang et al., 2018), while the interlayer tuff of the slate has been dated to the Late Carboniferous (Gong et al., 2021). Therefore, we temporarily define the Dashizhai Formation as a diachronic stratum, with the formation age between the Late Carboniferous and the Early Permian. Volcanic rocks theoretically serve as sources of sulfur and pre-enrichments of metals through magmatic-hydrothermal processes before the primary metallogenic epoch (Heinrich and Candela, 2014; Kissin and Mango, 2014). Therefore, identifying the magmatic-hydrothermal process is crucial for understanding the metallogenic mechanism of the Shuangjiazishan Ag-Pb-Zn deposit. However, detailed reports on the magmatic-hydrothermal alteration of the extremely thick slate are scarce in previous studies.

This study focuses on the Late Carboniferous extremely thick slate in the Shuangjiazishan basin. We investigate the rock-forming mineral assemblages and generations, whole-rock geochemical characteristics, sulfide mineral types, and genesis to unveil mineral phase changes and magmatic-hydrothermal alteration characteristics. We compare mineral and fracture content differences between the "black" slate and the "green" slate, emphasizing the limitation of slate as a host rock for mineralization horizons. Combined with the previous studies, we discuss and propose a depositional model for the slate.

## 2 Geological background

The Shuangjiazishan-Wusinihei area is situated in the northeastern segment of the XMOB, with the South Mongolia microcontinent to the north and the NCC to the south (Figure 1A). The regional geological evolution is relatively complex. It was controlled by the Paleo-Asian Oceanic tectonic system in the Paleozoic and was superimposed and reworked by the Mongolia-Okhotsk Oceanic tectonic system and the Paleo-Pacific Oceanic tectonic system in the Mesozoic (Şengör et al., 1993; Xiao et al., 2009; Xiao et al., 2018). Several Late Paleozoic sedimentary and intrusive rocks are exposed in the area (Figure 1B). The major lithostratigraphic units include the Benbatu Formation, Amushan Formation, Dashizhai Formation, Zhesi Formation, and Linxi Formation. The distribution of the Carboniferous units is relatively limited (Zhao et al., 2016; Zhu et al., 2017). The Upper Carboniferous Benbatu Formation consists of sandstone and mudstone, with occurrences of carbonate and volcanic rocks. The Upper Carboniferous Amushan Formation is overlying the Benbatu Formation, with a small number of siliciclastic rocks in addition to carbonate rocks. The Permian rocks are widespread in the area. The Upper Carboniferous-Lower Permian Dashizhai Formation mainly comprises bimodal volcanic and pyroclastic rocks (Zhang et al., 2008). The dominant lithologies are rhyolite and dacite, with lesser amounts of basalt and andesite. The Middle Permian Zhesi Formation, known for the Zhesi fauna, consists of shallow marine carbonate rocks and sandstone (Wang et al., 2004). The Upper Permian Linxi Formation occupies an area with about 4,000 m thick continental conglomerate and shale deposits (Mueller et al., 1991). The fault structure is relatively developed in this area, generally trending in the NE direction, which controls the distribution of rock masses and ore bodies. The later superimposed NW-NEW and NNE striking secondary faults create favorable structural traps for mineralization.

The Shuangjiazishan ore district is located approximately 20 km northwest of Fuhe Town, Balinzuo Banner, Inner Mongolia Autonomous Region. It can be divided into the Shuangjiazishan and Xinglongshan ore sections (Figure 2). The two ore sections are approximately 4.7 km apart, with the Xinglongshan ore section exhibiting higher ore grades compared to the Shuangjiazishan ore section.

### 2.1 Stratigraphic setting of the ore district

The lithostratigraphic units exposed in the ore district include the following formations:

The Upper Carboniferous-Lower Permian Dashizhai Formation (C<sub>2</sub>-P<sub>1d</sub>): This volcano-sedimentary unit is extensively distributed in the ore district. It strikes along the NE direction and dips toward the NW at an angle of approximately 55–65°. It has a thickness exceeding 950 m and is overlain by the Middle Jurassic Xinmin Formation with an angular unconformity contact. The Dashizhai Formation can be divided into upper and lower lithologic sections. The upper section mainly consists of black slate and dark gray metamorphic siltstone, while the lower section primarily comprises brown-gray altered andesite mixed with dark gray andesite tuff.

The Middle Jurassic Xinmin Formation (J<sub>2x</sub>): The unit is distributed in the southeast of the Xinglongshan ore section, and

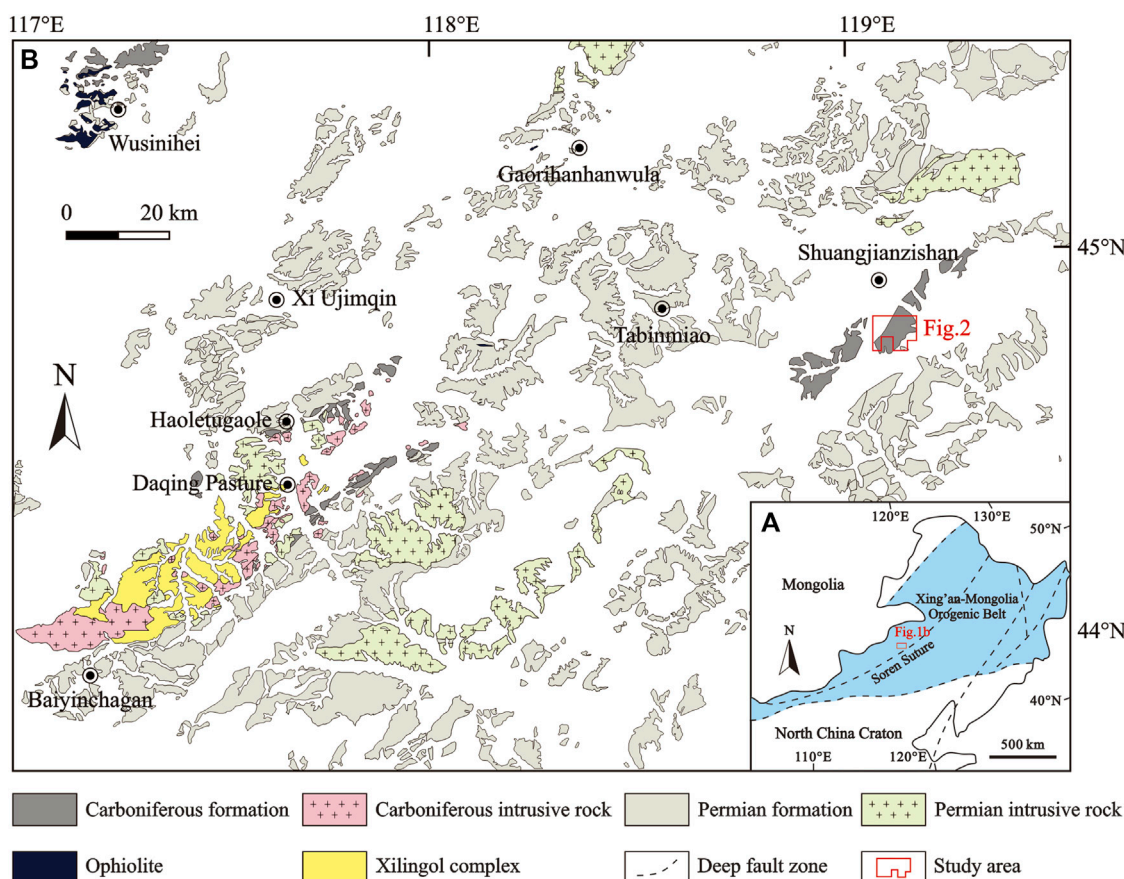


**FIGURE 1** Tectonic location map (A) and geological sketch (B) of the Shuangjianzishan-Wusinihei area (modified after Gong et al., 2021).

has a thickness exceeding 165 m. It is in angular unconformity contact with the Dashizhai Formation, and parallel unconformable contact with the Upper Jurassic Manketou Obo Formation. Similar to the Dashizhai Formation, the Xinmin Formation can also be divided into upper and lower lithologic sections. The upper lithologic section is mainly yellow-brown rhyolitic breccia tuff, while the lower section consists of dark gray conglomerate, fine sandstone, and siltstone mixed with carbonaceous mudstone and thin coal line.

The Upper Jurassic Manketou Orbo Formation ( $J_3m$ ): The unit is mainly exposed in the Shuangjianzishan area, northwest of the ore district, with a thickness of more than 480 m. It is in angular unconformity contact with the Dashizhai Formation. Only the lower lithologic section of the Manketou Orbo Formation is exposed, mainly composed of grey-yellow tuffaceous sandstone and rhyolitic breccia tuff mixed with grey-yellow greywacke.

The Quaternary Holocene ( $Q_4$ ): This unit consists of loose accumulations of sandy loam soil scattered in the foothills and gentle slopes of the ore district, with a thickness ranging from about 0.3–6.0 m. Sand gravels are scattered in valleys of the ore district, which are poorly sorted, accumulated in disorder, mostly sub-angular or sub-rounded, with a thickness of about 10.0–38.3 m.

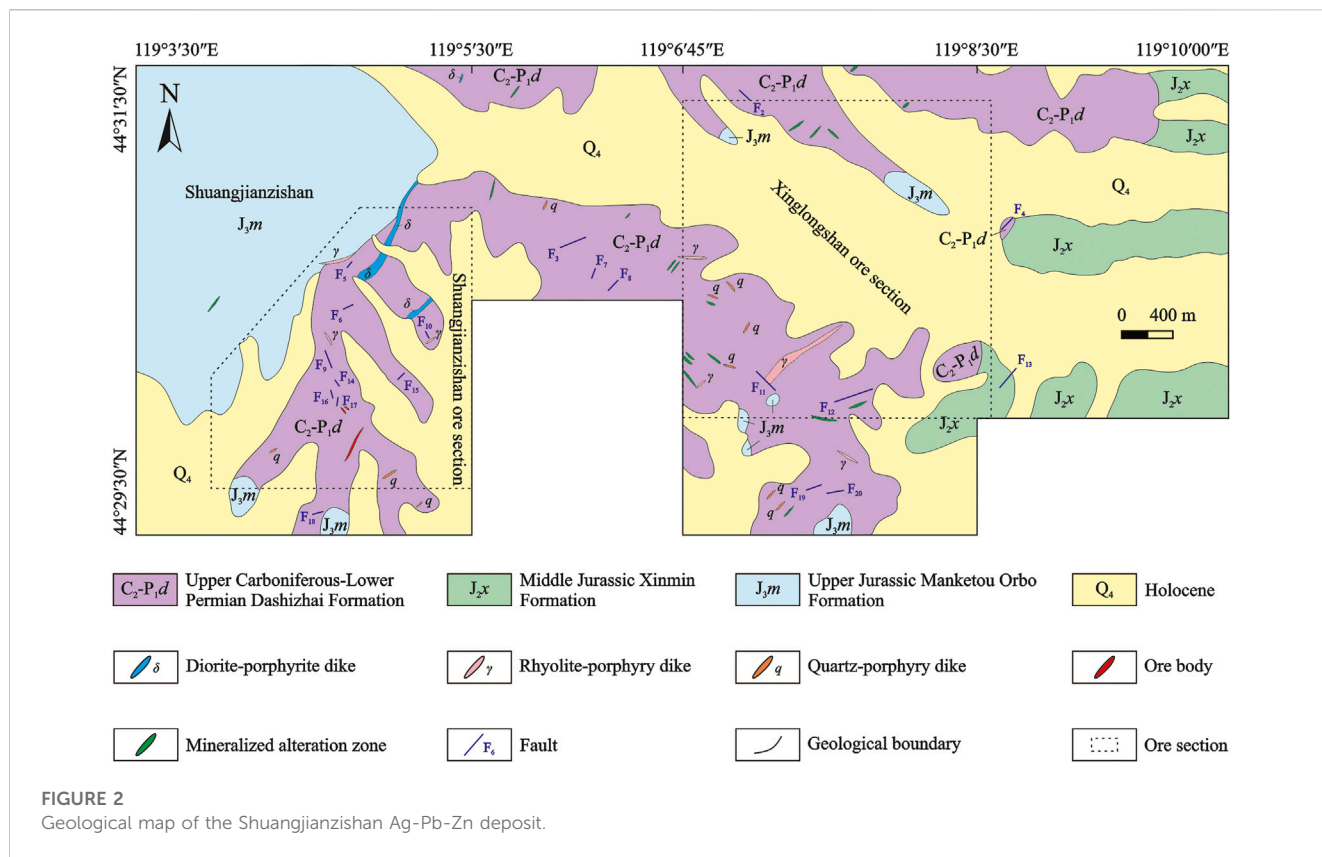
## 2.2 Structural setting of the ore district

The ore district is situated in the NW limb of the Yaerya-Pangjiawan compound anticline, which is a regional fold structure with a NE strike. The Dashizhai Formation exhibits a general monoclinial attitude. Within the ore district, several structures are present, including NW-striking ductile shear zones, NE-striking faults, NW-striking faults, and nearly NS-striking faults. These faults are important ore-controlling and ore-hosting structures. Based on the intersection relationship between the fault structures, it is inferred that the NW-striking ductile shear zone formed during the Early Mesozoic period, followed by the development of NE and NW striking faults. The nearly NS-striking faults are the youngest among them, cutting across the NE and NW striking faults.

## 2.3 Magmatic rocks of the ore district

The magmatic rocks exposed in the ore district include the following types:

Diorite-porphyrite dikes: These dikes are mainly exposed on the surface in the western part of the ore district, while they are concealed in the eastern part. They exhibit a gray-green color,



porphyritic texture, and massive structure. The phenocrysts within these dikes are mainly composed of plagioclase and amphibole. The matrix consists of microcrystalline plagioclase and a small amount of granular quartz, containing disseminated pyrite, sphalerite, and scattered galena. Liu et al. (2016) have determined intrusion ages of  $254 \pm 3$  Ma and  $252 \pm 3$  Ma, indicating that the diorite-porphyrity dikes were formed during the Indosinian magmatic event.

**Rhyolite-porphyrity dikes:** These dikes are only exposed in the eastern part of the ore district. They have a brown-yellow color, porphyritic texture, and rhyolitic structure. The phenocrysts within these dikes primarily consist of quartz and potassium feldspar. The matrix is composed of microcrystalline plagioclase and ferruginous cement. The formation age of rhyolite-porphyrity dikes is determined to be  $169 \pm 3$  Ma (Liu et al., 2016).

**Granite bodies:** Most of the granite bodies in the ore district are concealed and in intrusive contact with the Dashizhai Formation. They exhibit a granule (or equigranular) texture and massive structure. Locally, crevices are developed within the granite bodies, which are filled with molybdenite veins. The rock-forming minerals in these bodies mainly include potassium feldspar, plagioclase, quartz, and biotite. Liu et al. (2016) have determined the emplacement age of  $130 \pm 6$  Ma, indicating that the granite bodies were formed during the Yanshanian magmatic event.

**Quartz-porphyrity dikes:** These dikes are intersected by ore bodies in underground mineworks. The dikes near the ore body display strong alteration, including greisenization, pyritization, and sphaleritization, while those farther away from the ore body retain a

relatively fresh state with an obvious porphyritic texture. Wu et al. (2013) have determined the intrusion age of  $239.08 \pm 0.94$  Ma, indicating that the quartz-porphyrity dikes were formed during the Indosinian magmatic event.

### 3 Sample description

The Dashizhai Formation in proximity to the Shuangjianzishan ore district exhibits a notable occurrence of slate, forming an exceptionally thick layer with a thickness of 8–10 m. We observed the typical outcrop ( $119^{\circ}9'59.03''E$ ,  $42^{\circ}21'28.86''N$ ) from a distance. The rock was dark gray to gray-black, the surface of which was seriously weathered (Figure 3A). When we stripped the exposed weathering surface ( $118^{\circ}58'49.19''E$ ,  $44^{\circ}27'59.29''N$ ) in a nearby outcrop, it can be seen that the rock was broken into blocks along joints, having a lot of iron rust spots on the surface (Figure 3B). For analysis purposes, we obtained samples from the Xinglongshan ore section ( $119^{\circ}6'45''E$ – $119^{\circ}8'30''E$ ,  $44^{\circ}29'30''N$ – $44^{\circ}31'30''N$ ) through drilling, specifically including ZK1501, ZK1601, and ZK1620. Taking the drilling core ZK1601 as an example, we noted the obvious black-green alternation characteristics (Figure 3C), suggesting that the composition of the slate may not be uniform. Consequently, we selected the “black” slate and the “green” slate from different depths, extracted rock blocks, and ground the powder after polishing, to make rock thin slices and conduct the whole-rock geochemical analysis.

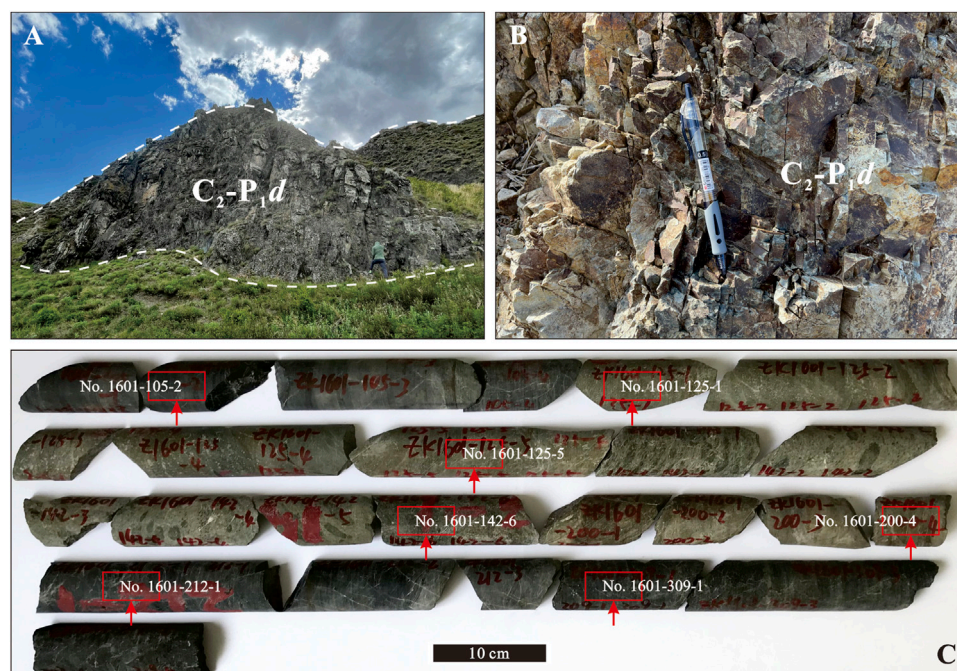


**FIGURE 3**

Photographs of typical field outcrops and drilling cores of the slate in the Shuangjianzishan basin. (A) The typical outcrop; (B) The typical weathered surface; (C) The representative drilling core (No. ZK1601). The sampling positions and numbers have been marked with red squares.

## 4 Methods

### 4.1 Mineral assemblages analysis

The mineral assemblages analysis was conducted at the MOE Key Laboratory of Orogenic Belts and Crustal Evolution, School of Earth and Space Sciences, Peking University, Beijing, China. We utilized a Nikon Eclipse LV100NPOL polarizing microscope and an FEI Quanta-650FEG scanning electron microscope (SEM) equipped with an Oxford INCA X-Max50 energy dispersive spectrometry (EDS) to examine the mineral assemblages in rock thin slices.

### 4.2 Whole-rock major and trace elements analysis

The chemical pretreatment and analysis of major and trace elements in the whole-rock samples were conducted at the Nanjing FocuMS Technology Company Limited, Jiangsu, China. For major elements, we adopt the acid dissolution method to dissolve the sample powder to analyze the major elements excluding Si, and the alkali fusion method to liquate the sample powder to analyze Si. The analytical instrument was an Agilent 5110 ICP-OES. The analysis accuracy of SiO<sub>2</sub> was better than 1%, that of Al<sub>2</sub>O<sub>3</sub>, TFe<sub>2</sub>O<sub>3</sub>, MgO, K<sub>2</sub>O, Na<sub>2</sub>O, and CaO was better than 3%, and that of TiO<sub>2</sub>, MnO, and P<sub>2</sub>O<sub>5</sub> was better than 5%. For trace elements, we adopt the acid dissolution method to dissolve the sample powder. The analytical instrument was an Agilent 7700x ICP-MS. The analysis accuracy of

trace elements with content more than 50 μg/g is better than 5%, that of trace elements with content between 5 μg/g and 50 μg/g is better than 10%, and that of trace elements with content between 0.5 μg/g and 5 μg/g is better than 20%. To ensure measurement quality, geochemical reference materials BHVO-2 and AGV-2 were treated as blind samples, and their measured values were compared with Geological and Environmental Reference Materials (GeoReM, Jochum and Nohl, 2008). The detailed operating procedures were conducted as described by Chen et al. (2017b).

### 4.3 Whole-rock sulfur content analysis

The chemical pretreatment and analysis of sulfur content in whole-rock samples were conducted at the ALS Chemex (Guangzhou) Company Limited, Guangdong, China. We adopt the oxidation method and used the induction furnace together with the infrared spectrum (IRS) to experiment. The LECO CS844 infrared carbon-sulfur analyzer served as the analytical instrument. The sample was placed in an induction furnace and subjected to combustion at 1,350°C. Sulfur was released in the form of sulfur dioxide, which then entered the IRS with the carrier gas to absorb infrared energy at a specific wavelength. The absorbed energy is proportional to the sulfur concentration, allowing for measurement of the whole-rock sulfur content based on energy changes received by the detector. The detection range for sulfur was 0.01–50 wt.%. The relative deviation for control accuracy was better than 3.54%, while the relative deviation for control precision was better than 5%.

## 4.4 *In-situ* sulfur isotope analysis of pyrites

The *in-situ* sulfur isotope analysis of sulfide was conducted at the Wuhan SampleSolution Analytical Technology Company Limited, Hubei, China. The analytical instrument was a Neptune Plus MC-ICP-MS equipped with a Geolas HD excimer ArF laser ablation system. Helium was used as the carrier gas in the laser ablation system. Single spot ablation mode was used with a large spot size of 44  $\mu\text{m}$ , a slow pulse frequency of 2 Hz, and a constant laser fluence of 5 J/cm<sup>2</sup>. Each analysis consisted of 100 laser pulses. A new signal-smoothing device was utilized to ensure stable signals, particularly under the slow pulse frequency condition (Hu et al., 2015). The Neptune Plus was equipped with nine Faraday cups fitted with 10<sup>11</sup>  $\Omega$  resistors. Isotopes <sup>32</sup>S, <sup>33</sup>S, and <sup>34</sup>S were collected in Faraday cups using static mode. The instrument was equipped with a newly designed X skimmer cone and Jet sample cone to improve signal intensity. Nitrogen gas (4 mL/min) was added to the central gas flow to reduce polyatomic interferences. A standard-sample bracketing (SSB) method was employed to correct for instrumental mass fractionation, using pyrite standard PPP-1 as the reference material to correct for the matrix effect in natural pyrite samples. The reference value of  $\delta^{34}\text{S}_{\text{V-CDT}}$  in the standard and further details of the *in-situ* sulfur isotope analysis can be found in Fu et al. (2016). All data reduction was performed using the “Iso-Compass” software (Zhang et al., 2020).

## 4.5 TESCAN integrated mineral analyzer (TIMA) analysis

Automatic identification of mineral phases and microstructures was conducted at the MOE Key Laboratory of Orogenic Belts and Crustal Evolution, School of Earth and Space Sciences, Peking University, Beijing, China. The analytical instrument was a TESCAN integrated mineral analyzer (TIMA), comprising a TESCAN Mira Schottky field emission SEM with four silicon drift EDS detectors arranged at 90° intervals around the chamber (Hrstka et al., 2018). The high-resolution liberation analysis mode was utilized. Backscattered electron (BSE) images were obtained to identify individual particles and boundaries between distinct preliminary phases. A rectangular mesh of measurements on each distinct phase was obtained using X-ray spectra. The system matches the spectroscopic data with mineral definition files, allowing for mineral identification and mapping. The volume and mass ratios of all mineral phases were automatically calculated. The measurements were performed at 25 kV using a spot size of ~110 nm, a working distance of 15 mm, and a field size set at 1,500  $\mu\text{m}$ .

# 5 Results

## 5.1 Petrographic characteristics

The slate is of blastopelitic texture, aphanitic texture, and shaly structure. Its sedimentary particles consist of quartz, feldspar, biotite, rock fragment, and clay minerals. Quartz can be classified into two types: primary quartz and secondary quartz. The primary

quartz appears as xenomorphic granules, with a size of less than 50  $\mu\text{m}$ , scattered within the calcareous cement (Figure 4A). Secondary quartz, on the other hand, is predominantly observed as veins and granules (Figure 4B), with a significantly larger size compared to primary quartz. The maximum size of secondary quartz can reach 250  $\mu\text{m}$ . It exhibits weakly oriented branched quartz veinlets and often displays a chaotic surface due to hydrothermal alteration (Figure 4C), with no apparent interference color. Feldspar appears irregular with unclear boundaries, and its surface appears light brown due to clavization. Biotite is yellow-brown in color, lacking normal pleochroism, and commonly occurs as aggregates with secondary quartz (Figure 4D). Both secondary quartz and biotite are products of hydrothermal alteration. The rock fragments, black and opaque, fill the gaps between other sedimentary particles. The interstitial materials mainly consist of calcareous and carbonaceous cement, which are challenging to distinguish under a polarizing microscope.

## 5.2 Whole-rock geochemical characteristics

### 5.2.1 Major elements

The whole-rock major element analytical results of the slate are listed in Supplementary Table S1. The loss on ignition (LOI) of all samples is generally high, ranging from 2.35 wt.% to 4.43 wt.%, with an average value of 3.22 wt.%. The high LOI may be related to the high content of organic matter. The SiO<sub>2</sub> content ranges from 58.40 wt.% to 71.19 wt.%, with an average value of 65.37 wt.%. The Al<sub>2</sub>O<sub>3</sub> content ranges from 12.30 wt.% to 17.99 wt.%, with an average value of 15.52 wt.%. The TFe<sub>2</sub>O<sub>3</sub> content ranges from 2.87 wt.% to 7.63 wt.%, with an average value of 5.08 wt.%. The K<sub>2</sub>O content ranges from 1.94 wt.% to 7.05 wt.%, with an average value of 4.07 wt.%. The geochemical classification diagram for sedimentary rocks indicates that the samples mainly fall within the wacke and shale areas (Figure 5A; Herron, 1988).

### 5.2.2 Trace elements

The whole-rock trace element analytical results of the slate are listed in Supplementary Table S2. The primitive mantle normalized spider diagram reveals that all samples exhibit similar right-dipping curve characteristics (Figure 5B). They are enriched in some large ion lithophile elements (LILE; such as Rb and K) while being depleted in high field strength elements (HFSE; such as Ta, Nb, P, and Ti).

The slate demonstrates a high total rare earth elements ( $\Sigma\text{REE}$ ) content, ranging from 102.0  $\mu\text{g/g}$  to 167.0  $\mu\text{g/g}$ , suggesting possible variations in the sedimentary geochemical environment. The average  $\Sigma\text{REE}$  content is 144.3  $\mu\text{g/g}$ , slightly lower than that of the North American shale (173.2  $\mu\text{g/g}$ ). The light rare earth element (LREE) content ranges from 89.34  $\mu\text{g/g}$  to 147.6  $\mu\text{g/g}$ , with an average of 128.0  $\mu\text{g/g}$ . The heavy rare earth element (HREE) content ranges from 12.61  $\mu\text{g/g}$  to 23.07  $\mu\text{g/g}$ , with an average of 16.29  $\mu\text{g/g}$ . The LREE/HREE ratio varies from 6.24 to 8.92, indicating differentiation between LREE and HREE. The average LREE/HREE ratio is 7.89, higher than that of North American shale (7.44; Haskin et al., 1966). The chondrite-normalized REE patterns also display similar right-dipping curve characteristics for all samples (Figure 5C), accompanied by a pronounced negative Eu

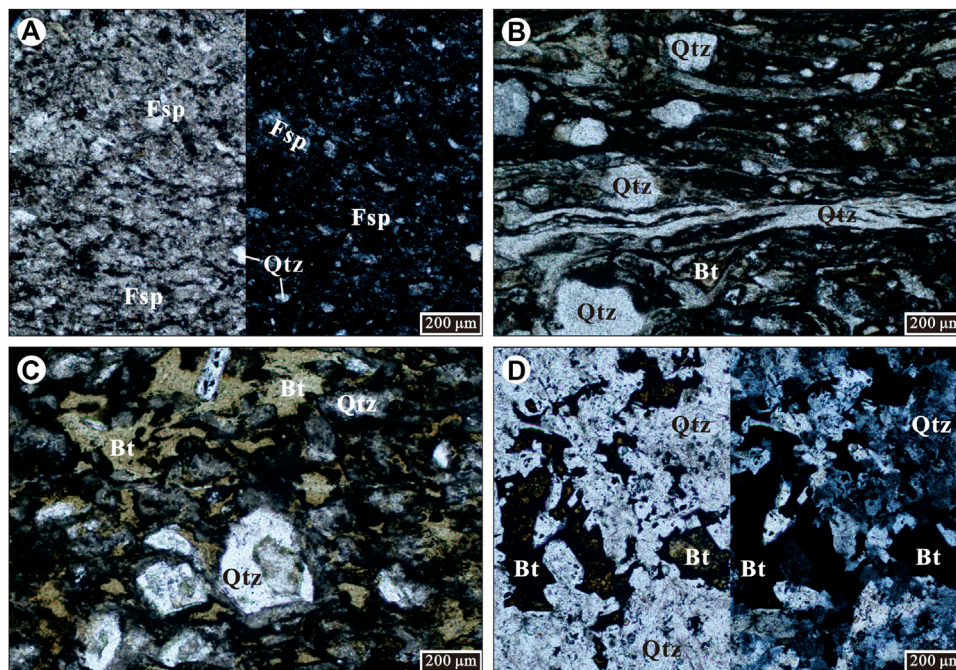


**FIGURE 4**

Typical micrographs of the slate in the Shuangjianzhan basin. (A) The primary quartz and feldspar (No. 1601-105-2), under plane/cross-polarized light; (B) The secondary quartz veins and particles (No. 1601-142-6), under plane-polarized light; (C) The secondary quartz and biotite affected by hydrothermal alteration (No. 1601-125-1), under plane-polarized light; (D) The secondary quartz and biotite aggregates (No. 1601-200-4), under plane/cross-polarized light. Mineral abbreviations: Bt-biotite; Fsp-feldspar; Qtz-quartz.

anomaly and LREE enrichment, but without a negative Ce anomaly. The North American shale-normalized REE patterns demonstrate a weak positive Eu anomaly, and an indistinct Ce anomaly, and generally exhibit horizontal or slightly left-dipping curves (Figure 5D).

### 5.3 Mineralogical characteristics of sulfide minerals

The whole-rock sulfur content analytical results of the slate are listed in [Supplementary Table S1](#). The sulfur content ranges from 0.01 wt.% to 0.91 wt.%, with an average of 0.11 wt.%. The sulfur content shows minor variation among individual samples. Microscopic observations reveal that the sulfide minerals present in the slate are primarily sphalerite and pyrite, with chalcopyrite and galena occurring less frequently.

**Sphalerite (ZnS):** It appears xenomorphic to subhedral, gray to dark brown, and exhibits a greasy luster under reflected light. Based on morphological differences, two types of sphalerite can be distinguished: vein sphalerite and irregular speckled sphalerite. Vein sphalerite is predominantly found within slate fissures, cutting through the carbonaceous cement, with a maximum size of 3.5 mm (Figure 6A). It contains enclosed xenomorphic galena (PbS) particles, typically around 5 μm in size. Irregular speckled sphalerite is dispersed within the cement of slate and generally ranges in size from 30 to 50 μm (Figure 6B). It also contains enclosed xenomorphic galena. Some vein sphalerites exhibit inclusions of

chalcopyrite (CuFeS<sub>2</sub>), which appears golden yellow with a metallic luster under the reflected light (Figure 6C). Chalcopyrite often occurs disseminated throughout the samples, indicating typical hydrothermal mineral characteristics.

**Pyrite (FeS<sub>2</sub>):** It appears yellow-white to light yellow, with a metallic luster under reflected light. Pyrite is scattered within the carbonaceous cement in the form of irregular speckled or subhedral cubic crystals (Figure 6D). The size ranges from 40 μm to 60 μm. There is no obvious relationship of generation among pyrite crystals, suggesting a possible hydrothermal origin. The *in-situ* sulfur isotope analytical results of pyrite in the slate are listed in [Supplementary Table S3](#). The pyrite δ<sup>34</sup>S<sub>V-CDT</sub> values exhibit minor variations, ranging from -1.41‰ to -0.09‰, all of which are negative. The average value is -0.62‰.

## 6 Discussions

### 6.1 Genesis of the slate

#### 6.1.1 Provenance analysis

The Al<sub>2</sub>O<sub>3</sub> content of sedimentary rocks can provide insights into their provenance, as it is controlled by the input of terrigenous clastic materials and is relatively resistant to diagenesis and metamorphism. In this case, the Al<sub>2</sub>O<sub>3</sub>/TiO<sub>2</sub> ratio of the samples ranges from 21.38 to 25.44 suggesting that the slate is likely derived from felsic rocks (Girty et al., 1996). The lg (La/Yb)-lgΣREE diagram, often used for reconstructing the original rock

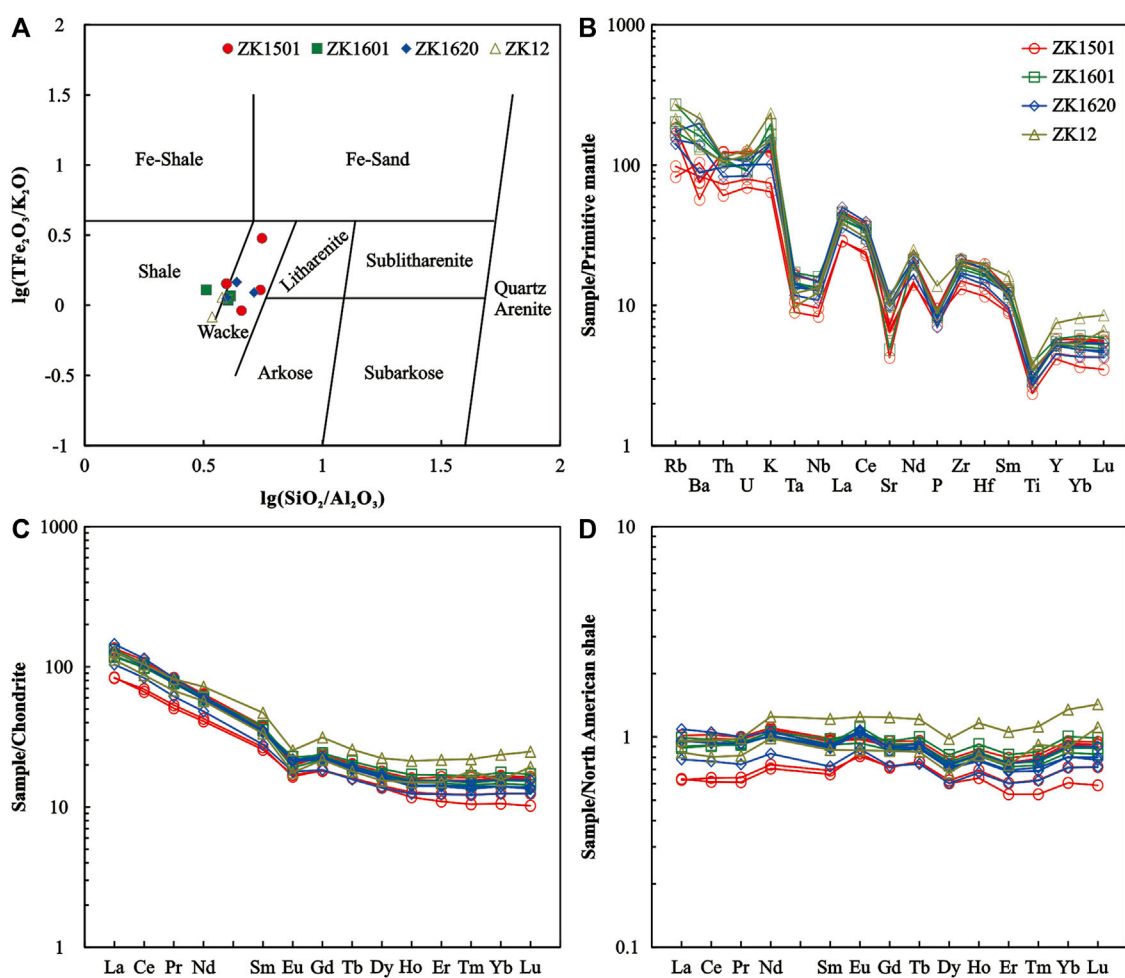


FIGURE 5

Major and trace element geochemical diagrams of the slate in the Shuangjianzishan basin. (A) The chemical classification diagram of clastic rocks (after Herron, 1988); (B) The primitive mantle normalized spider diagram; (C) The chondrite normalized REE patterns diagram; (D) The North American shale normalized REE patterns diagram. Normalized values of the primitive mantle and the chondrite were cited from Sun and McDonough (1989). Normalized values of the North American shale were cited from Gromet et al. (1984). The whole-rock major and trace element data of the drilling cores ZK12 were cited from Gong et al. (2021).

characteristics of sedimentary rocks (Zhu and Wang, 1994), shows that most samples fall within the clastic field, with a few samples overlapping with the continental tholeiite field (Figure 7A). Additionally, the  $\text{SiO}_2\text{-Al}_2\text{O}_3$  diagram indicates that the samples fall within the seawater deposit area (Figure 7B). These observations suggest that the slate is likely a seawater deposition and has not undergone significant transformation due to large-scale hydrothermal or biological processes.

### 6.1.2 Hydrothermal activity analysis

The redox state of sedimentary water can influence the differentiation and enrichment of elements, which is often recorded in sedimentary rocks. Selecting appropriate geochemical indicators is crucial for qualitatively assessing the redox state of sedimentary water (Meyer et al., 2012; Maslov and Podkovyrov, 2018). The La/Ce ratio can be used to determine whether sedimentary rocks have been influenced by hydrothermal fluids. A La/Ce ratio equal to 2.80 suggests ancient seawater or

hydrothermal crust influence, while a ratio of 0.25 indicates normal Fe-Mn deposition. Ratios less than 1.00 suggest hydrothermal fluid influence during sediment formation (Toth, 1980). In the case of the slate samples, the La/Ce ratio ranges from 0.45 to 0.50, which is less than 1.00, indicating hydrothermal alteration during their formation (Figure 7C). The presence of vein sphalerite, galena, and chalcopyrite inclusions in sphalerite further supports the occurrence of hydrothermal activity.

Regarding the sulfur isotopes, four reservoirs exist in nature: mantle-derived sulfur, modern seawater sulfur, marine sulfate in geological periods, and bioreduction sulfur (Mao et al., 2003). The  $\delta^{34}\text{S}$  variation range for mantle-derived sulfur is  $0\text{‰} \pm 3\text{‰}$  (Chaussidon and Lorand, 1990). In this case, the average  $\delta^{34}\text{S}_{\text{V-CDT}}$  value of pyrites in the samples is  $-0.62\text{‰}$ , which does not significantly change with depth. Combined with the mineralogical characteristics, these scattered pyrites are most likely pre-enriched metals formed before the primary metallogenic epoch.

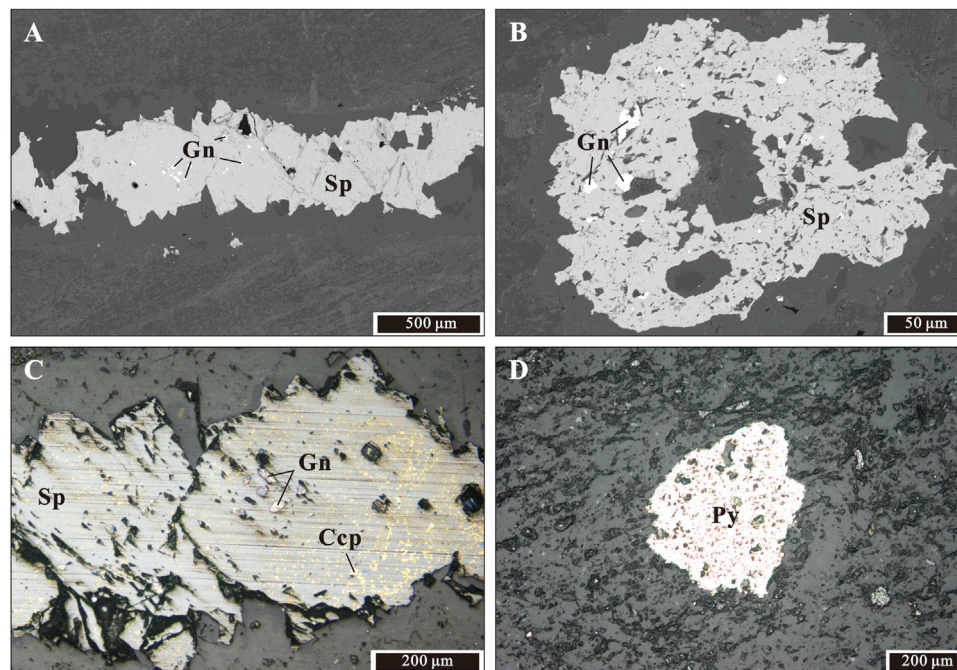


**FIGURE 6**

Typical micrographs of sulfide minerals in the slate from the Shuangjanzishan basin. (A) The vein sphalerite (No. 1601-105-2), under the SEM; (B) The irregular speckled sphalerite (No. 1601-309-1), under the SEM; (C) The galena and chalcopyrite inclusions in sphalerite (No. 1601-212-1), under reflected light; (D) The subhedral speckled pyrite (No. 1601-125-1), under reflected light. Mineral abbreviations: Ccp-chalcopyrite; Gn-galena; Py-pyrite; Sp-sphalerite.

Arsenic enrichment is an important indicator for distinguishing hydrothermal depositions from seawater depositions (Marchig et al., 1982; Boström, 1983). All the samples exhibit As enrichment, with varying content ranging from 1.36  $\mu\text{g/g}$  to 20.13  $\mu\text{g/g}$  and an average value of 8.95  $\mu\text{g/g}$ . This suggests that the As enrichment in the slate is a result of hydrothermal activity.

### 6.1.3 Sedimentary environment analysis

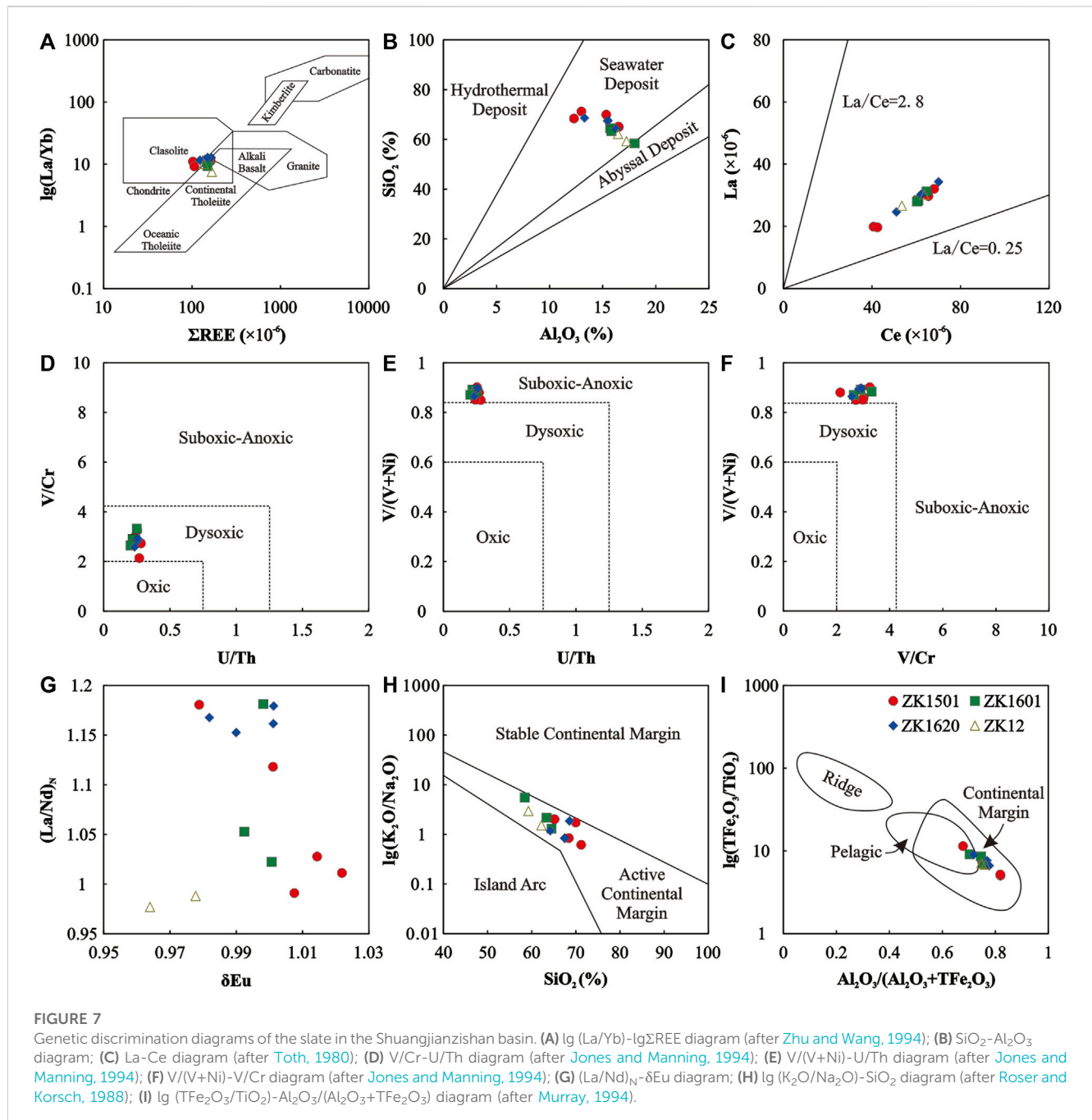
To assess the pale-oxygenation facies of sedimentary water, sensitive elements such as V, Cr, U, Th, and Ni are considered (Wingnall, 1994; Kimura and Watanabe, 2001; Tribovillard et al., 2006). Common geochemical indicators include the V/Cr ratio, U/Th ratio, and V/(V+Ni) ratio, among others. Generally, a V/Cr ratio below 2.00 indicates oxic deposition, a ratio between 2.00 and 4.25 indicates dysoxic deposition and a ratio above 4.25 indicates suboxic-anoxic deposition; A U/Th ratio below 0.75 indicates oxic deposition, a ratio between 0.75 and 1.25 indicates dysoxic deposition and a ratio above 1.25 indicates suboxic-anoxic deposition; A V/(V+Ni) ratio value below 0.60 indicates oxic deposition, a ratio between 0.60 and 0.84 indicates dysoxic deposition and a ratio above 0.84 indicates suboxic-anoxic deposition (Jones and Manning, 1994). To accurately determine the redox state of sedimentary water, bivariate parameters were used to plot pale-oxygenation facies diagrams. In this case, all the samples fall within the dysoxic deposition area of the V/Cr-U/Th diagram (Figure 7D), and they fall within the suboxic-anoxic deposition area of the V/(V+Ni)-U/Th and V/(V+Ni)-V/Cr diagrams (Figures 7E, F). Therefore, it can be inferred that the slate in the

Shuangjanzishan basin was deposited in an oxygen-deficient environment typical of a shale basin.

### 6.1.4 Europium anomaly analysis

Europium exists predominantly in the form of  $\text{Eu}^{2+}$  in strongly reducing or alkaline seawater, while it mainly exists as  $\text{Eu}^{3+}$  in oxic seawater. Seawater deposition usually exhibits no or weak Eu anomaly. The presence of abundant organic matter in an oxygen-deficient environment can lead to the reduction of  $\text{Eu}^{3+}$  to  $\text{Eu}^{2+}$  during burial diagenesis, followed by re-migration. The burial diagenesis process can affect the Eu anomaly of sedimentary rocks, and a decrease in the  $(\text{La}/\text{Nd})_{\text{N}}$  ratio is often observed with enhanced burial diagenesis (Shields and Stille, 2001). However, there is no obvious correlation between the  $(\text{La}/\text{Nd})_{\text{N}}$  ratio and the  $\delta\text{Eu}$  value (Figure 7G) in the samples, indicating that burial diagenesis has not altered the REE compositions of the slate.

A weak Eu-positive anomaly is observed in the North American shale-normalized REE patterns diagram (Figure 5D). An Eu-positive anomaly in marine sediments is generally attributed to two conditions: the addition of calcium-rich volcanic ash during deposition or the influence of high-temperature-reducing hydrothermal fluids rich in  $\text{Eu}^{2+}$  during deposition (Douville et al., 1999). In the slate samples from the Shuangjanzishan basin, interlayer tuff has been identified (Gong et al., 2021), suggesting that the Eu-positive anomaly may be related to the addition of calcium-rich volcanic ash and hydrothermal activity. It is proposed that the slate was formed in seawater under the influence of magmatic-hydrothermal fluids (Owen et al., 1999). The value of  $\delta\text{Eu}$  reflects the degree of influence.



### 6.1.5 Tectonic environment analysis

The formation and evolution of sedimentary basins are determined by regional tectonic settings. Tectonic activities control the provenance, transportation, diagenesis process of sediments, and chemical conditions of the sedimentary medium. Therefore, the migration and enrichment of elements in the strata are closely related to the regional tectonic setting. The geochemical composition of sedimentary rocks can be used to reflect the regional tectonic setting and its evolution characteristics. In the case of the samples, all of them fall within the active continental margin area of the  $\lg(K_2O/Na_2O)$ - $SiO_2$  diagram ([Figure 7H](#); [Roser and Korsch, 1988](#)) and the continental margin area of the  $\lg(TFe_2O_3/TiO_2)$ -

$Al_2O_3/(Al_2O_3+TFE_2O_3)$  diagram ([Figure 7I](#); [Murray, 1994](#)). These observations are consistent with the Paleozoic tectonic system of the XMOB.

### 6.2 Color changes of the slate

The color changes observed in the slate can be attributed to variations in mineral composition and microstructure. At the field outcrop scale, the slate appears extremely thick ([Figure 3A](#)) and has dense cement ([Figure 3B](#)). In hand specimens, the drilling core of the slate exhibits alternating transitions between black and green

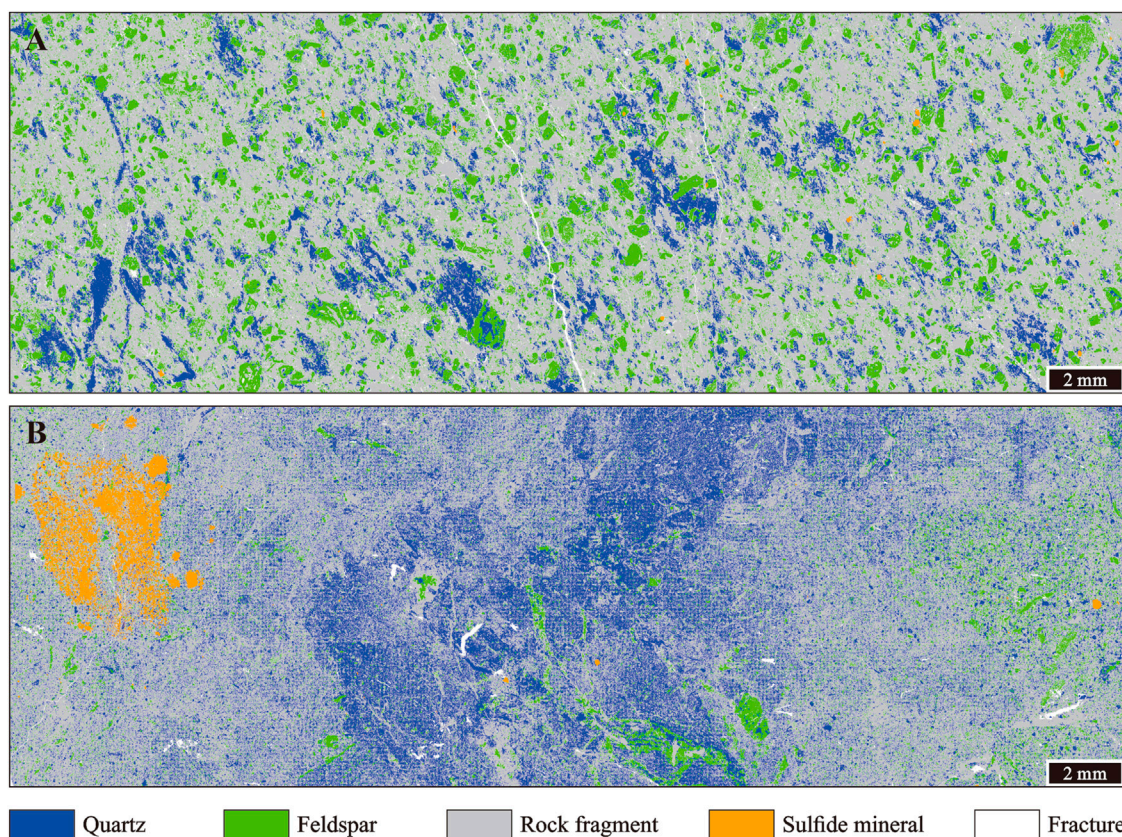


**FIGURE 8**

Microstructure and mineral assemblage of the slate in the Shuangjianshan basin. (A) TIMA mineral phases distribution of the “green” slate (No. 1601-125-1); (B) TIMA mineral phases distribution of the “black” slate (No. 1601-212-1).

without apparent patterns (Figure 3C). This suggests that the composition of slates may not be uniform, and there are variations in mineral phases. To analyze the differences in mineral assemblage and microstructure, thin slices of typical “green” slate (No. 1601-125-1) and “black” slate (No. 1601-212-1) for TIMA analysis. The analysis considered quartz, feldspar, rock fragments, and sulfide minerals, while the proportion of altered minerals (e.g., clays, chlorite) was converted back to their original minerals.

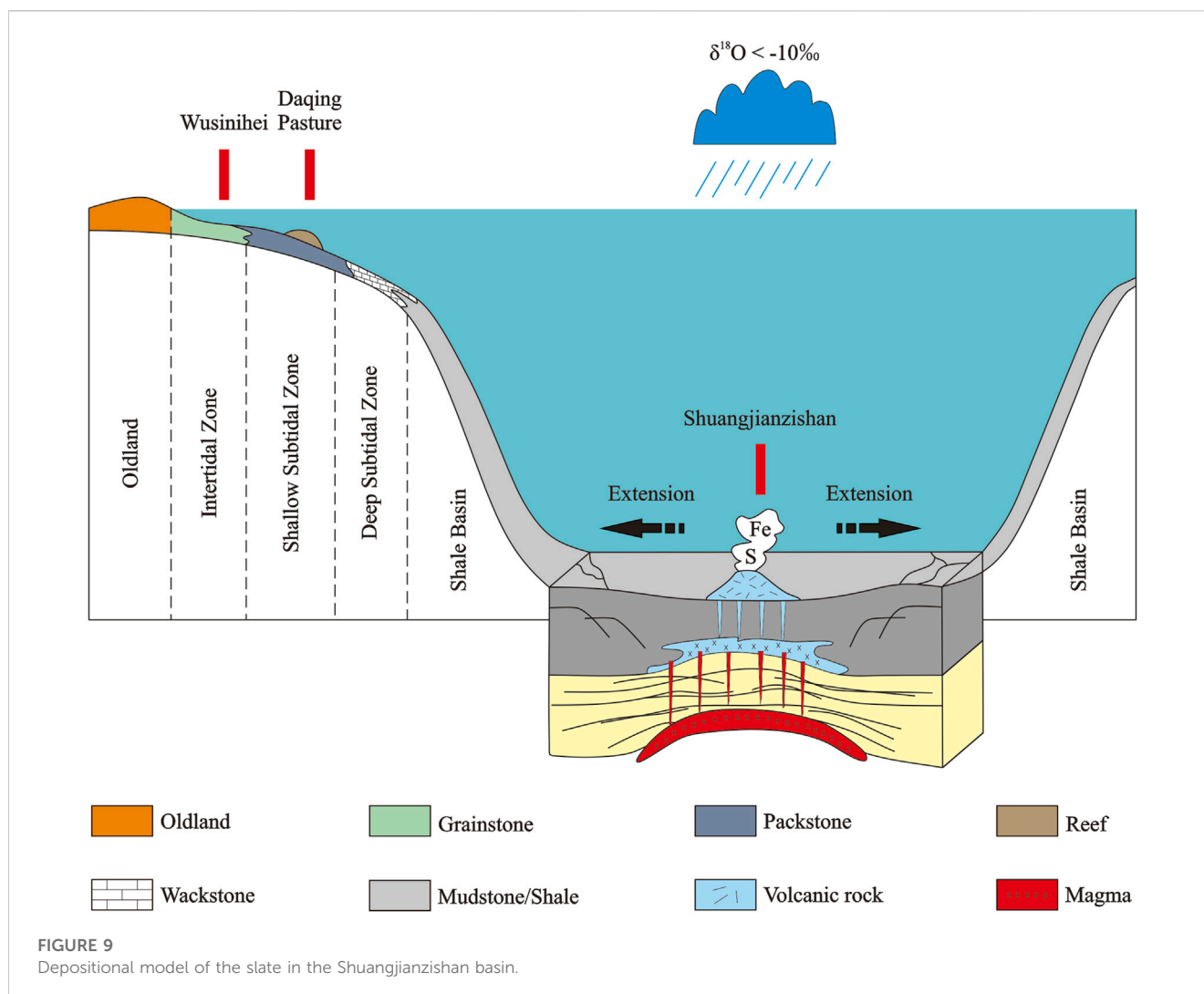
The mineral phase analysis results of the typical “green” slate are shown in Figure 8A, in which quartz content is about 10.08 vol.%, feldspar content is about 14.42 vol.%, rock fragment content is about 72.27 vol.%, sulfide minerals content is about 0.09 vol.%, and fracture content is about 3.14 vol.%. As the content of feldspar in the “green” slate is slightly higher than that of quartz, and feldspar is easily weathered in the supergene environment, the slate surface is greenish. The mineral phase analysis results of the typical “black” slate are shown in Figure 8B, in which quartz content is about 25.03 vol.%, feldspar content is about 4.50 vol.%, rock fragment content is about 67.22 vol.%, sulfide minerals content is about 2.41 vol.%, and fracture content is about 0.84 vol.%.

Comparatively, the highest content component in both the “green” and “black” slate is the rock fragment, resulting in the overall dark gray to black appearance in the field outcrop. The

alternation of slate color from black to green can be attributed to the difference in feldspar content, potentially influenced by the addition of calcium-rich volcanic ash during the sedimentary process. This leads to compositional heterogeneity in the slate. The “black” slate, with slightly higher sulfide minerals content and significantly lower fracture content, indicates denser characteristics that are not conducive to the migration of magmatic-hydrothermal fluids. As a result, sulfide minerals are locally enriched in the “black” slate, explaining why the slate of the Dashizhai Formation can serve as the host rock for the Shuangjianshan Ag-Pb-Zn deposit.

### 6.3 Depositional model analysis of the slate

The Late Paleozoic tectonic system of the XMOB has been a subject of debate, with conflicting views regarding whether it was characterized by “extension” or “subduction”. Previous studies have primarily focused on intrusive rocks and bimodal volcanic rocks exposed in the XMOB and the northern margin of the NCC (e.g., Zhang et al., 2007; Zhang et al., 2009a; Zhang et al., 2009b; Jian et al., 2010; Xu et al., 2013; Zhang et al., 2014; Li et al., 2016; Zhang et al., 2016; Li et al., 2017; Xu et al., 2018; Zhou et al., 2019), with limited research on sedimentation. Scholars advocating the “extension” view have proposed that the Carboniferous-Permian sedimentary rocks



in the XMOB primarily originated in the marine-continental transition zone, without significant deep ocean basin deposition (Shao et al., 2014; Xu et al., 2018). However, proponents of the “subduction” view have discovered radiolarian fossils in Middle Permian mudstones from the Xilinhot area (Shang, 2004). They argue that a vast ocean existed in the Late Paleozoic of the XMOB, supporting the occurrence of deep ocean sedimentation. Nevertheless, Fang et al. (2014) found gastropod and bivalve fossils associated with the Permian radiolarian fossils in the same location and horizon, suggesting that these radiolarians may not have originated from the deep ocean basin and that the existence of a “Permian Ocean” is uncertain.

Different tectonic environments often give rise to distinct sedimentary characteristics, including particle size, sedimentation rate, and bedding dip angles, which can provide insights into the dynamic background of deposition. Continental rift basin subsidence typically involves slow uplift of the surrounding denudation zone, and the presence of active faults creates a stable and abundant supply of materials for the sedimentation process, resulting in minor deformation of the deposited layers. Consequently, continental rift sedimentation

generally exhibits finer particle sizes, higher sedimentation rates, and stable stratum dip angles. In the Shuangjiazishan basin, these characteristics are exemplified by the occurrence of extremely thick slate. Petrographic observations reveal that the primary mineral particle sizes are all within 50  $\mu\text{m}$ , making it challenging to distinguish mineral assemblages and cement types under a polarizing microscope. Through zircon U-Pb dating and Monte Carlo simulation, Gong et al. (2021) have constrained the maximum duration of the 2030 m thick strata in the Shuangjiazishan basin to 6.9 Ma. They have also determined that the minimum sedimentation rate of the slate is 294 m/Myr, equivalent to the lacustrine sedimentation rate observed in the East African Rift Zone (Bourrouilh, 1987; Eberli and Ginsburg, 1987; Einsele, 2000) and much higher than that of forearc basins (Doubleday et al., 1993; Vannucchi et al., 2003; Butterworth, 2009; Rains et al., 2012). Furthermore, the stratum dipping angles calculated from drilling data consistently indicate a stable angle of 60°, suggesting that the slate was deposited in a relatively stable sedimentary environment without significant deformation. Based on these findings, it is preliminarily concluded that the

sedimentary tectonic environment of the slate in the Shuangjiazishan basin bears a strong resemblance to that of a continental rift lake.

The carbonate-clastic rocks represented by the Late Carboniferous Benbatu Formation and Amushan Formation were widely developed in XMOB, and no lithologic assemblage represented the deep ocean basin depositions. Zhao et al. (2016) revealed that the XMOB had entered a stable epicontinental sea sedimentary stage in the Late Carboniferous by systematically studying the stratigraphic sequence, fossil assemblages, sedimentary structures, and material sources of different typical profiles. Based on the petrological and geochemical characteristics of the slate in the Shuangjiazishan basin, it is inferred that the slate was formed in oxygen-deficient seawater during the Late Carboniferous. The volcanic ash released by the continental rift crater during the post-orogenic extension of the Paleo-Asian Ocean contributed to the deposition process, resulting in the interlayer tuff observed in the slate (Figure 9). Previous studies on the zircon oxygen isotope composition of the interlayer tuff indicate wide variations in  $\delta^{18}\text{O}$  values, mostly lower than the mantle value ( $5.3\text{‰} \pm 0.3\text{‰}$ ; Valley et al., 2005). This may be attributed to the remelting of hydrothermally altered rocks in the continental rift (Gong et al., 2021). The lithosphere stretching caused by the continental rift setting enhances the subterranean heat and provides enough heat for the magma-wallrock reaction so that the surface water can penetrate the depth of at least 10–15 km, and then a notable high-temperature water-rock reaction occurs (Bindeman, 2008; Watts et al., 2011; Drew et al., 2013). During the Mesozoic, the Shuangjiazishan basin was influenced by the Mongolia-Okhotsk Oceanic tectonic system and the Paleo-Pacific tectonic system. Epithermal magmatic-hydrothermal fluids altered the slate, leading to the formation of secondary quartz, biotite, and various sulfide minerals. The “black” slate represents a mineralized layer, likely acting as a chemical trap for ores due to its redox features (e.g., carbonaceous matter, and pyrite). Following the mineralizing phase, the slate became cemented by ore and gangue minerals, significantly reducing its permeability. Localized mineralization occurred in fractures, resulting in the formation of the Shuangjiazishan Ag-Pb-Zn deposit (Zhai et al., 2020).

## 7 Concluding remarks

In conclusion, based on the petrographic characteristics, whole-rock geochemical data, and sulfide mineral types and genesis of the Late Carboniferous extremely thick slate from the Shuangjiazishan basin in the eastern CAOB, the following conclusions can be drawn.

1. The Shuangjiazishan extremely thick slate represents oxygen-deficient seawater deposition during the Late Carboniferous, with the involvement of volcanic ash. It has undergone alteration by epithermal magmatic-hydrothermal fluids.
2. The slate exhibits alternating color changes from black to green in drilling cores. The denser “black” slate marks the metallogenic horizon of the Shuangjiazishan super-large Ag-Pb-Zn deposit.

## Data availability statement

The original contributions presented in the study are included in the article/Supplementary Material, further inquiries can be directed to the corresponding authors.

## Author contributions

WT, Y-HZ, and ZL designed the research plan. W-PZ, WT, Y-HZ, and C-JW collected the samples on field trips. W-PZ, M-YG, BF, and Z-LW analyzed the samples. W-PZ wrote the original manuscript. Y-HZ and ZL revised the original manuscript. Y-HZ provided the funding. All authors contributed to the article and approved the submitted version.

## Funding

The research was funded by the National Key Research and Development Program of China (Grant Nos. 2018YFE0204202, 2017YFC0601302, and 2017YFC0601305), the National Natural Science Foundation of China (Grant Nos. 42030304 and 42072224) and the China Geological Survey (Grant Nos. DD20221649 and DD20221647).

## Acknowledgments

We thank the Associate Editor Prof. Costanza Bonadiman and two reviewers for their constructive comments that greatly improved the original manuscript.

## Conflict of interest

Author M-YG was employed by SINOPEC.

The remaining authors declare that the research was conducted in the absence of any commercial or financial relationships that could be construed as a potential conflict of interest.

## Publisher's note

All claims expressed in this article are solely those of the authors and do not necessarily represent those of their affiliated organizations, or those of the publisher, the editors and the reviewers. Any product that may be evaluated in this article, or claim that may be made by its manufacturer, is not guaranteed or endorsed by the publisher.

## Supplementary material

The Supplementary Material for this article can be found online at: <https://www.frontiersin.org/articles/10.3389/feart.2023.1145656/full#supplementary-material>

## References

- Bindeman, I. (2008). Oxygen isotopes in mantle and crustal magmas as revealed by single crystal analysis. *Rev. Mineralogy Geochem.* 69, 445–478. doi:10.2138/rmg.2008.69.12
- Boström, K. (1983). “Genesis of ferromanganese deposits—diagnostic criteria for recent and old deposits,” in *Hydrothermal processes at seafloor spreading centers* (Boston: Springer), 473–489.
- Bourrouilh, R. (1987). Evolutionary mass flow-megaturbidites in an interplate basin: Example of the North Pyrenean basin. *Geo-Marine Lett.* 7, 69–81. doi:10.1007/bf02237986
- Butterworth, P. J. (2009). “The role of eustasy in the development of a regional shallowing event in a tectonically active basin: Fossil bluff group (Jurassic-Cretaceous), Alexander island, Antarctica,” in *Sedimentation, tectonics and eustasy: Sea-level changes at active margins* (Oxford: Special Publications of the International Association of Sedimentologists Blackwell Publishing Limited), 1307–1329.
- Chaussidon, M., and Lorand, J. P. (1990). Sulphur isotope composition of orogenic spinel ilherzolite massifs from Ariège (North-Eastern Pyrenees, France): An ion microprobe study. *Geochimica Cosmochimica Acta* 54, 2835–2846. doi:10.1016/0016-7037(90)90018-g
- Chen, Y. J., Zhang, C., Wang, P., Pirajno, F., and Li, N. (2017a). The Mo deposits of northeast China: A powerful indicator of tectonic settings and associated evolutionary trends. *Ore Geol. Rev.* 81, 602–640. doi:10.1016/j.oregeorev.2016.04.017
- Chen, S., Wang, X. H., Niu, Y. L., Sun, P., Duan, M., Xiao, Y. Y., et al. (2017b). Simple and cost-effective methods for precise analysis of trace element abundances in geological materials with ICP-MS. *Sci. Bull.* 62, 277–289. doi:10.1016/j.scib.2017.01.004
- Doubleday, P. A., Macdonald, D. I. M., and Nell, P. A. R. (1993). Sedimentology and structure of the trench-slope to forearc basin transition in the Mesozoic of Alexander Island, Antarctica. *Geol. Mag.* 130, 737–754. doi:10.1017/s0016756800023128
- Douville, E., Bienvenu, P., Charlou, J. L., Donval, J. P., Fouquet, Y., Appriou, P., et al. (1999). Yttrium and rare Earth elements in fluids from various deep-sea hydrothermal systems. *Geochimica Cosmochimica Acta* 63, 627–643. doi:10.1016/s0016-7037(99)00024-1
- Drew, D. L., Bindeman, I. N., Watts, K. E., Schmitt, A. K., Fu, B., and McCurry, M. (2013). Crustal-scale recycling in caldera complexes and rift zones along the yellowstone hotspot track: O and Hf isotopic evidence in diverse zircons from voluminous rhyolites of the picabo volcanic field, Idaho. *Earth Planet. Sci. Lett.* 381, 63–77. doi:10.1016/j.epsl.2013.08.007
- Eberli, G. P., and Ginsburg, R. N. (1987). Segmentation and coalescence of cenozoic carbonate platforms, northwestern Great bahama bank. *Geology* 15, 75. doi:10.1130/0091-7613(1987)15<75:saccoc>2.0.co;2
- Einsle, G. (2000). *Sedimentary basins: Evolution, facies, and sediment budget*. Springer, 792.
- Fang, J. Q., Zhao, P., Xu, B., Shao, J. A., and Wang, Y. (2014). Sedimentary facies analyses and discovery of gastropods from Zhesi Formation in the south of West Ujimqin, Inner Mongolia and their significances. *Acta Petrol. Sin.* 30, 1889–1898. (in Chinese with English abstract).
- Fu, J. L., Hu, Z. C., Zhang, W., Yang, L., Liu, Y. S., Li, M., et al. (2016). *In situ* sulfur isotopes ( $\delta^{34}\text{S}$  and  $\delta^{33}\text{S}$ ) analyses in sulfides and elemental sulfur using high sensitivity cones combined with the addition of nitrogen by Laser Ablation MC-ICP-MS. *Anal. Chim. Acta* 911, 14–26. doi:10.1016/j.aca.2016.01.026
- Gao, J., Klemd, R., Zhu, M. T., Wang, X. S., Li, J. L., Wan, B., et al. (2018). Large-scale porphyry-type mineralization in the central asian metallogenic domain: A review. *J. Asian Earth Sci.* 165, 7–36. doi:10.1016/j.jseas.2017.10.002
- Girty, G. H., Ridge, D. L., Knaack, C., Johnson, D., and Al-Riyami, R. K. (1996). Provenance and depositional setting of Paleozoic chert and argillite, Sierra Nevada, California. *J. Sediment. Res.* 66, 107–118. doi:10.1306/D42682CA-2B26-11D7-864800102C1865D
- Gong, M. Y., Zhang, Y. H., Tian, W., and Fu, B. (2021). Depositional age and Genesis of the host strata of the Shuangjianzishan Ag-Pb-Zn deposit: Implications for the Late Carboniferous magmatic-hydrothermal activities and tectonic evolution of the eastern central Asia orogenic belt. *Ore Geol. Rev.* 135, 104207. doi:10.1016/j.oregeorev.2021.104207
- Gromet, L. P., Haskin, L. A., Korotev, R. L., and Dymek, R. F. (1984). The “North American shale composite”: Its compilation, major and trace element characteristics. *Geochimica Cosmochimica Acta* 48, 2469–2482. doi:10.1016/0016-7037(84)90298-9
- Haskin, L. A., Wildeman, T. R., Frey, F. A., Collins, K. A., Keedy, C. R., and Haskin, M. A. (1966). Rare earths in sediments. *J. Geophys. Res.* 71, 6091–6105. doi:10.1029/jz071i024p06091
- Heinrich, C. A., and Candela, P. A. (2014). “Fluids and ore formation in the Earth’s crust,” in *Treatise on geochemistry*. Second Edition (Oxford: Elsevier), 1–28.
- Herron, M. M. (1988). Geochemical classification of terrigenous sands and shales from core or log data. *J. Sediment. Petrology* 58, 820–829. doi:10.1306/212F8E77-2B24-11D7-864800102C1865D
- Hrstka, T., Gottlieb, P., Skála, R., Breiter, K., and Motl, D. (2018). Automated mineralogy and petrology-applications of TESCAN integrated mineral analyzer (TIMA). *J. Geosciences* 63, 47–63. doi:10.3190/jgeosci.250
- Hu, Z. C., Zhang, W., Liu, Y. S., Gao, S., Li, M., Zong, K. Q., et al. (2015). “Wave” signal-smoothing and mercury-removing device for laser ablation quadrupole and multiple collector ICPMS analysis: Application to lead isotope analysis. *Anal. Chem.* 87, 1152–1157. doi:10.1021/ac503749k
- Jian, P., Liu, D. Y., Kröner, A., Windley, B. F., Shi, Y. R., Zhang, W., et al. (2010). Evolution of a permian intraoceanic arc-trench system in the solonker suture zone, central asian orogenic belt, China and Mongolia. *Lithos* 118, 169–190. doi:10.1016/j.lithos.2010.04.014
- Jochum, K. P., and Nohl, U. (2008). Reference materials in geochemistry and environmental research and the GeoReM database. *Chem. Geol.* 253, 50–53. doi:10.1016/j.chemgeo.2008.04.002
- Jones, B., and Manning, D. A. (1994). Comparison of geochemical indices used for the interpretation of palaeoredox conditions in ancient mudstones. *Chem. Geol.* 111, 111–129. doi:10.1016/0009-2541(94)90085-x
- Ke, L. L., Zhang, H. Y., Liu, J. J., Zhai, D. G., Guo, D. H., Yang, J. K., et al. (2017). Fluid inclusion, HO, S, Pb and noble gas isotope studies of the Aerhada Pb-Zn-Ag deposit, Inner Mongolia, NE China. *Ore Geol. Rev.* 88, 304–316. doi:10.1016/j.oregeorev.2017.05.012
- Kimura, H., and Watanabe, Y. (2001). Oceanic anoxia at the Precambrian-Cambrian boundary. *Geology* 29, 995–998. doi:10.1130/0091-7613(2001)029<0995:oaatpc>2.0.co;2
- Kissin, S. A., and Mango, H. (2014). “Silver vein deposits,” in *Treatise on geochemistry*. Second Edition (Oxford: Elsevier), 425–432.
- Li, S., Chung, S. L., Wilde, S. A., Wang, T., Xiao, W. J., and Guo, Q. Q. (2016). Linking magmatism with collision in an accretionary orogen. *Sci. Rep.* 6, 25751–25812. doi:10.1038/srep25751
- Li, S., Chung, S. L., Wilde, S. A., Jahn, B. M., Xiao, W. J., Wang, T., et al. (2017). Early-Middle triassic high Sr/Y granitoids in the southern central asian orogenic belt: Implications for ocean closure in accretionary orogens. *J. Geophys. Res. Solid Earth* 122, 2291–2309. doi:10.1002/2017jb014006
- Liu, C. H., Bagas, L., and Wang, F. X. (2016). Isotopic analysis of the super-large Shuangjianzishan Pb-Zn-Ag deposit in Inner Mongolia, China: Constraints on magmatism, metallogenesis, and tectonic setting. *Ore Geol. Rev.* 75, 252–267. doi:10.1016/j.oregeorev.2015.12.019
- Mao, J. W., Li, X. F., Zhang, R. H., Wang, Y. T., He, Y., and Zhang, Z. H. (2003). *Mantle-derived fluid-related ore-forming system*. Beijing: Geological Publishing House, 1–365. (in Chinese).
- Mao, J. W., Pirajno, F., Lehmann, B., Luo, M. C., and Berzina, A. (2014). Distribution of porphyry deposits in the Eurasian continent and their corresponding tectonic settings. *J. Asian Earth Sci.* 79, 576–584. doi:10.1016/j.jseas.2013.09.002
- Marchig, V., Gundlach, H., Möller, P., and Schley, F. (1982). Some geochemical indicators for discrimination between diagenetic and hydrothermal metalliferous sediments. *Mar. Geol.* 50, 241–256. doi:10.1016/0025-3227(82)90141-4
- Maslov, A. V., and Podkovyrov, V. N. (2018). Ocean redox state at 2500–500 Ma: Modern concepts. *Lithology Mineral Resour.* 53, 190–211. doi:10.1134/s0024490218030057
- Meyer, E. E., Quicksall, A. N., Landis, J. D., Link, P. K., and Bostick, B. C. (2012). Trace and rare Earth elemental investigation of a Sturtian cap carbonate, Pocatello, Idaho: Evidence for ocean redox conditions before and during carbonate deposition. *Precambrian Res.* 192, 89–106. doi:10.1016/j.precamres.2011.09.015
- Mueller, J. F., Rogers, J. J. W., Jin, Y. G., Wang, H. Y., Li, W. G., Chronic, J., et al. (1991). Late carboniferous to permian sedimentation in inner Mongolia, China, and tectonic relationships between north China and siberia. *J. Geol.* 99, 251–263. doi:10.1086/629487
- Murray, R. W. (1994). Chemical criteria to identify the depositional environment of chert: General principles and applications. *Sediment. Geol.* 90, 213–232. doi:10.1016/0037-0738(94)90039-6
- Ouyang, H. G., Mao, J. W., Santosh, M., Wu, Y., Hou, L., and Wang, X. F. (2014a). The Early Cretaceous Weilasituo Zn-Cu-Ag vein deposit in the southern Great Xing’an Range, northeast China: Fluid inclusions, H, O, S, Pb isotope geochemistry and genetic implications. *Ore Geol. Rev.* 56, 503–515. doi:10.1016/j.oregeorev.2013.06.015
- Ouyang, H. G., Xu, X., Mao, J. W., Su, H. M., Santosh, M., Zhou, Z. H., et al. (2014b). The nature and timing of ore formation in the budunhua copper deposit, southern Great xing’an range. *Acta Geol. Sin. Engl. Ed.* 88, 29–30. doi:10.1111/1755-6724.12367\_15
- Ouyang, H. G., Mao, J. W., Zhou, Z. H., and Su, H. M. (2015). Late Mesozoic metallogeny and intracontinental magmatism, southern Great Xing’an Range, northeastern China. *Gondwana Res.* 27, 1153–1172. doi:10.1016/j.gr.2014.08.010
- Owen, A. W., Armstrong, H. A., and Floyd, J. D. (1999). Rare Earth element geochemistry of upper ordovician cherts from the southern uplands of scotland. *J. Geol. Soc.* 156, 191–204. doi:10.1144/gsjgs.156.1.0191

- Rains, J. L., Marsaglia, K. M., and Dunne, G. C. (2012). Stratigraphic record of subduction initiation in the Permian metasedimentary succession of the El Paso Mountains, California. *Lithosphere* 4, 533–552. doi:10.1130/1165.1
- Roser, B. P., and Korsch, R. J. (1988). Provenance signatures of sandstone-mudstone suites determined using discriminant function analysis of major-element data. *Chem. Geol.* 67, 119–139. doi:10.1016/0009-2541(88)90010-1
- Ruan, B. X., Lv, X. B., Yang, W., Liu, S. T., Yu, Y. M., Wu, C. M., et al. (2015). Geology, geochemistry and fluid inclusions of the Bianjiadayuan Pb-Zn-Ag deposit, Inner Mongolia, NE China: Implications for tectonic setting and metallogeny. *Ore Geol. Rev.* 71, 121–137. doi:10.1016/j.oregeorev.2015.05.004
- Sengor, A. M. C., Natal'in, B. A., and Burtman, V. S. (1993). Evolution of the Altaid tectonic collage and Palaeozoic crustal growth in Eurasia. *Nature* 364, 299–307. doi:10.1038/364299a0
- Shang, Q. H. (2004). Occurrences of Permian radiolarians in central and eastern Inner Mongolia and their geological significance to the Northern China Orogen. *Chin. Sci. Bull.* 49, 2574–2579. (in Chinese).
- Shao, J. A., Tang, K. D., and He, G. Q. (2014). Early Permian tectono-palaeogeographic reconstruction of inner Mongolia, China. *Acta Petrol. Sin.* 30, 1858–1866. (in Chinese with English abstract).
- Shields, G., and Stille, P. (2001). Diagenetic constraints on the use of cerium anomalies as palaeoseawater redox proxies: An isotopic and REE study of Cambrian phosphorites. *Chem. Geol.* 175, 29–48. doi:10.1016/s0009-2541(00)00362-4
- Shu, Q. H., Chang, Z. S., Lai, Y., Zhou, Y. T., Sun, Y., and Yan, C. (2016). Regional metallogeny of Mo-bearing deposits in northeastern China, with new Re-Os dates of porphyry Mo deposits in the northern Xilamulun district. *Econ. Geol.* 111, 1783–1798. doi:10.2113/econgeo.111.7.1783
- Sun, S. S., and McDonough, W. F. (1989). Chemical and isotopic systematics of oceanic basalts: Implications for mantle composition and processes. *Geol. Soc. Lond. Spec. Publ.* 42, 313–345. doi:10.1144/gsl.sp.1989.042.01.19
- Sun, Q. F., Wang, K. Y., Sun, F. Y., Zhang, M., Zhao, C. G., and Sun, L. X. (2022). Fluid evolution and ore Genesis of Cu-Pb-Zn veins in the Panjiadian deposit, Great Xing'an Range, NE China: Evidence from fluid inclusion and H-O-He-Ar isotopes. *Geol. Mag.* 159, 1663–1680. doi:10.1017/s0016756822000425
- Toth, J. R. (1980). Deposition of submarine crusts rich in manganese and iron. *Geol. Soc. Am. Bull.* 91, 44–54. doi:10.1130/0016-7606(1980)91<44:doscri>2.0.co;2
- Tribouillard, N., Algeo, T. J., Lyons, T., and Riboulleau, A. (2006). Trace metals as paleoredox and paleoproductivity proxies: An update. *Chem. Geol.* 232, 12–32. doi:10.1016/j.chemgeo.2006.02.012
- Valley, J. W., Lackey, J. S., Cavosie, A. J., Clechenko, C. C., Spicuzza, M. J., Basei, M. A. S., et al. (2005). 4.4 billion years of crustal maturation: Oxygen isotope ratios of magmatic zircon. *Contributions Mineralogy Petrology* 150, 561–580. doi:10.1007/s00410-005-0025-8
- Vannucchi, P., Ranero, C. R., Galeotti, S., Straub, S. M., Scholl, D. W., and Mcdougall-Ried, K. (2003). Fast rates of subduction erosion along the Costa Rica Pacific margin: Implications for nonsteady rates of crustal recycling at subduction zones. *J. Geophys. Res.* 108, 2511. doi:10.1029/2002jb002207
- Wang, C. Y., Wang, P., and Li, W. G. (2004). Conodonts from the Permian Jisu honguer (Zhesi) formation of inner Mongolia, China. *Geobios* 37, 471–480. doi:10.1016/j.geobios.2003.06.003
- Wang, X. D., Wei, W., Lv, X. B., Fan, X. J., and Wang, S. B. (2018). Stanniferous magnetite composition from the Haobugao skarn Fe-Zn deposit, southern Great Xing'an Range: Implication for mineral depositional mechanism. *Geol. J.* 53, 1823–1839. doi:10.1002/gj.3009
- Wang, F. X., Bagas, L., Jiang, S. H., Zhang, F. X., Liu, Y. F., and Chong, X. X. (2019). Geochronology and ore Genesis of the shuangjianzishan Ag-polymetallic deposit, inner Mongolia, China. *Ore Geol. Rev.* 107, 1020–1045. doi:10.1016/j.oregeorev.2019.03.026
- Watts, K. E., Bindeman, I. N., and Schmitt, A. K. (2011). Large-volume rhyolite Genesis in caldera complexes of the snake river plain: Insights from the kilgore tuff of the heise volcanic field, Idaho, with comparison to yellowstone and bruneau-jarbridge rhyolites. *J. Petrology* 52, 857–890. doi:10.1093/petrology/egr005
- Wingnall, B. (1994). *Black shales*. Oxford: Clarendon Press, 120–152.
- Wu, G. B., Liu, J. M., Zeng, Q. D., Sun, H. S., and Liu, M. T. (2013). Age of mineralization in the Shuangjianzishan Pb-Zn-Ag deposit. *Acta Mineral. Sin.* 33, 619. (in Chinese).
- Xiao, W. J., Windley, B. F., Huang, B. C., Han, C. M., Yuan, C., Chen, H. L., et al. (2009). End-Permian to mid-Triassic termination of the accretionary processes of the southern Altai: Implications for the geodynamic evolution, Phanerozoic continental growth, and metallogeny of Central Asia. *Int. J. Earth Sci.* 98, 1189–1217. doi:10.1007/s00531-008-0407-z
- Xiao, W. J., Windley, B. F., Han, C. M., Liu, W., Wan, B., Zhang, J. E., et al. (2018). Late Paleozoic to early Triassic multiple roll-back and oroclinal bending of the Mongolia collage in Central Asia. *Earth-Science Rev.* 186, 94–128. doi:10.1016/j.earscirev.2017.09.020
- Xu, B., Charvet, J., Chen, Y., Zhao, P., and Shi, G. Z. (2013). Middle Paleozoic convergent orogenic belts in Western Inner Mongolia (China): Framework, kinematics, geochronology and implications for tectonic evolution of the Central Asian Orogenic Belt. *Gondwana Res.* 23, 1342–1364. doi:10.1016/j.gr.2012.05.015
- Xu, B., Wang, Z. W., Zhang, L. Y., Wang, Z. H., Yang, Z. N., and He, Y. (2018). The Xing'an-Mongolia intracontinent orogenic belt. *Acta Petrol. Sin.* 34, 2819–2844. (in Chinese with English abstract).
- Yang, Q. D., Guo, L., Wang, T., Zeng, T., Zhang, L., Tong, Y., et al. (2014). Geochronology, origin, sources and tectonic settings of Late Mesozoic two-stage granites in the Ganzhuermiao region, central and southern Da Hinggan Range, NE China. *Acta Petrol. Sin.* 30, 1961–1981. (in Chinese with English abstract).
- Yu, Q., Ge, W. C., Zhang, J., Zhao, G. C., Zhang, Y. L., and Yang, H. (2017). Geochronology, petrogenesis and tectonic implication of late paleozoic volcanic rocks from the Dashizhai Formation in inner Mongolia, NE China. *Gondwana Res.* 43, 164–177. doi:10.1016/j.gr.2016.01.010
- Zeng, Q. D., Liu, J. M., Zhang, Z. L., Chen, W. J., and Zhang, W. Q. (2011). Geology and geochronology of the Xilamulun molybdenum metallogenic belt in eastern Inner Mongolia, China. *Int. J. Earth Sci.* 100, 1791–1809. doi:10.1007/s00531-010-0617-z
- Zhai, D. G., Liu, J. J., Zhang, H. Y., Wang, J. P., Su, L., Yang, X. A., et al. (2014a). Origin of oscillatory zoned garnets from the xiერთალა Fe-Zn skarn deposit, northern China: In situ LA-ICP-MS evidence. *Lithos* 190, 279–291. doi:10.1016/j.lithos.2013.12.017
- Zhai, D. G., Liu, J. J., Zhang, H. Y., Yao, M. J., Wang, J. P., and Yang, Y. Q. (2014b). S-Pb isotopic geochemistry, U-Pb and Re-Os geochronology of the Huanggangliang Fe-Sn deposit, Inner Mongolia, NE China. *Ore Geol. Rev.* 59, 109–122. doi:10.1016/j.oregeorev.2013.12.005
- Zhai, D. G., Liu, J. J., Zhang, A. L., and Sun, Y. Q. (2017). U-Pb, Re-Os, and <sup>40</sup>Ar/<sup>39</sup>Ar geochronology of porphyry Sn±Cu±Mo and polymetallic (Ag-Pb-Zn-Cu) vein mineralization at Bianjiadayuan, inner Mongolia, northeast China: Implications for discrete mineralization events. *Econ. Geol.* 112, 2041–2059. doi:10.5382/econgeo.2017.4540
- Zhai, D. G., Liu, J. J., Zhang, H. Y., Tombros, S., and Zhang, A. L. (2018). A magmatic-hydrothermal origin for Ag-Pb-Zn vein formation at the Bianjiadayuan deposit, Inner Mongolia, NE China: Evidences from fluid inclusion, stable (CHO) and noble gas isotope studies. *Ore Geol. Rev.* 101, 1–16. doi:10.1016/j.oregeorev.2018.07.005
- Zhai, D. G., Williams-Jones, A. E., Liu, J. J., Selby, D., Voudouris, P. C., Tombros, S., et al. (2020). The Genesis of the giant Shuangjianzishan epithermal Ag-Pb-Zn deposit, Inner Mongolia, northeastern China. *Econ. Geol.* 115, 101–128. doi:10.5382/econgeo.4695
- Zhang, S. H., Zhao, Y., Song, B., Yang, Z. Y., Hu, J. M., and Wu, H. (2007). Carboniferous granitic plutons from the northern margin of the North China Block: Implications for a late Palaeozoic active continental margin. *J. Geol. Soc.* 164, 451–463. doi:10.1144/0016-76492005-190
- Zhang, X. H., Zhang, H. F., Tang, Y. J., Wilde, S. A., and Hu, Z. C. (2008). Geochemistry of Permian bimodal volcanic rocks from central inner Mongolia, north China: Implication for tectonic setting and Phanerozoic continental growth in central Asian orogenic belt. *Chem. Geol.* 249, 262–281. doi:10.1016/j.chemgeo.2008.01.005
- Zhang, S. H., Zhao, Y., Song, B., Hu, J. M., Liu, S. W., Yang, Y. H., et al. (2009a). Contrasting late carboniferous and late Permian-middle triassic intrusive suites from the northern margin of the North China Craton: Geochronology, petrogenesis, and tectonic implications. *Geol. Soc. Am. Bull.* 121, 181–200. doi:10.1130/b26157.1
- Zhang, S. H., Zhao, Y., Kröner, A., Liu, X. M., Xie, L. W., and Chen, F. K. (2009b). Early Permian plutons from the northern North China Block: Constraints on continental arc evolution and convergent margin magmatism related to the Central Asian Orogenic Belt. *Int. J. Earth Sci.* 98, 1441–1467. doi:10.1007/s00531-008-0368-2
- Zhang, S. H., Zhao, Y., Ye, H., Liu, J. M., and Hu, Z. C. (2014). Origin and evolution of the bainaimiao arc belt: Implications for crustal growth in the southern central Asian orogenic belt. *Geol. Soc. Am. Bull.* 126, 1275–1300. doi:10.1130/b31042.1
- Zhang, S. H., Zhao, Y., Liu, J. M., and Hu, Z. C. (2016). Different sources involved in generation of continental arc volcanism: The Carboniferous-Permian volcanic rocks in the northern margin of the North China Block. *Lithos* 240, 382–401. doi:10.1016/j.lithos.2015.11.027
- Zhang, X. F., Zhou, Y., Liu, J. L., Li, S. C., Wang, B. R., Teng, C., et al. (2018). Geochronology and geochemistry for volcanic rocks of Dashizhai Formation and its geological significance in xi ujimqin banner, inner Mongolia. *Acta Petrol. Sin.* 34, 1775–1791. (in Chinese with English abstract).
- Zhang, H. Y., Zhai, D. G., Liu, J. J., Li, P. L., Li, K., and Sun, H. J. (2019). Fluid inclusion and stable (H-O-C) isotope studies of the giant Shuangjianzishan epithermal Ag-Pb-Zn deposit, Inner Mongolia, NE China. *Ore Geol. Rev.* 115, 103170. doi:10.1016/j.oregeorev.2019.103170

Zhang, W., Hu, Z. C., and Liu, Y. S. (2020). Iso-Compass: New freeware software for isotopic data reduction of LA-MC-ICP-MS. *J. Anal. Atomic Spectrom.* 35, 1087–1096. doi:10.1039/d0ja00084a

Zhao, P., Xu, B., Tong, Q. L., Chen, Y., and Faure, M. (2016). Sedimentological and geochronological constraints on the Carboniferous evolution of central Inner Mongolia, southeastern Central Asian Orogenic Belt: Inland sea deposition in a postorogenic setting. *Gondwana Res.* 31, 253–270. doi:10.1016/j.gr.2015.01.010

Zhou, Z. H., Lv, L. S., Feng, J. R., Li, C., and Li, T. (2010). Molybdenite Re-Os ages of Huanggang skarn Sn-Fe deposit and their geological significance, Inner Mongolia. *Acta Petrol. Sin.* 26, 667–679. (in Chinese with English abstract).

Zhou, H., Zhao, G. C., Li, J. H., Han, Y. G., Yao, J. L., and Wang, B. (2019). Magmatic evidence for middle-late Permian tectonic evolution on the northern margin of the North China Craton. *Lithos* 336, 125–142. doi:10.1016/j.lithos.2019.04.002

Zhu, X. Q., and Wang, Z. G. (1994). “Geochemical characteristics of sediment at hot water region in the okinawa trough,” in *Study on geochemistry* (Beijing: Earthquake Publishing House), 108–112. (in Chinese).

Zhu, W. P., Tian, W., Wei, C. J., Shao, J. A., Fu, B., Fanning, C. M., et al. (2017). Late Paleozoic rift-related basalts from central Inner Mongolia, China. *J. Asian Earth Sci.* 144, 155–170. doi:10.1016/j.jseas.2017.04.007